Biosensors and Bioelectronics 127 (2019) 181–187

Contents lists available at ScienceDirect

Biosensors and Bioelectronics

journal homepage: www.elsevier.com/locate/bios

Bimetallic metal-organic frameworks derived cobalt nanoparticles embedded in nitrogen-doped carbon nanotube nanopolyhedra as advanced electrocatalyst for high-performance of activated carbon air-cathode microbial fuel cell

Song Zhang[a,b,1], Wei Su[a,1], Xiaojing Wang[a,*], Kexun Li[b,*], Yong Li[c]

[a] School of Chemical Engineering and Technology, Tianjin key Laboratory of Membrane and Desalination Technology, Tianjin University, Tianjin 300350, China
[b] The College of Environmental Science and Engineering, Tianjin Key Laboratory of environmental Remediation Pollution Control, MOE Key Laboratory of Pollution Processes and Environmental Criteria, Tianjin Key Laboratory of Environmental Technology for Complex Trans-Media Pollution, Nankai University, Tianjin 300071, China
[c] Trinity International Consulting Corporation, Beijing 100022, China

ARTICLE INFO

Keywords:
Carbon nanotube nanopolyhedra
Cobalt nanoparticles
Air cathode
Oxygen reduction reaction
Microbial fuel cell

ABSTRACT

A new type of nitrogen-doped carbon nanotube embedded cobalt nanoparticles nanopolyhedra (Co-NCNTNP) electrocatalyst synthesized via pyrolysis bimetallic metal-organic frameworks was investigated to modify the activated carbon air-cathode microbial fuel cell (MFC). X-ray diffraction and transmission electron microscope characterization confirmed the combination of nitrogen-doped carbon nanotube and transition metal element in Co-NCNTNP. Rotating disk electrode measurement revealed the oxygen reduction reaction (ORR) of as-prepared Co-NCNTNP was mainly proceeded via a four-electron pathway like Pt/C. When fabricated into activated carbon cathode, the optimized MFC reached the maximum power density of 2252 ± 46 mW m^{-2}, which was 154% higher than that of control. Moreover, the resistance including total resistance and charge transfer resistance of modified cathode significantly decreased comparing to the control, which was beneficial to better MFC performance. Therefore, all attracting properties suggested that noble-metal-free and high-efficiency Co-NCNTNP could be considered as a Pt-alternative electrocatalyst for ORR in MFC.

1. Introduction

With the increasing consumption of traditional fossil fuels and worsening global environmental pollution, microbial fuel cell (MFC) as a novel and green biological and energy recovery technology that directly utilizes bacteria to oxidize organic substances and generates electricity, has aroused wide research interest owing to its simple apparatus, room temperature operation condition, lower energy consumption and wastewater treatment capability (Fan et al., 2012; Qiao et al., 2010). However, previous research has identified that the low power density of MFC mainly resulting from the sluggish kinetics of the oxygen reduction reaction (ORR) on cathode greatly limited its practical application (Zhu et al., 2015). It is well known that noble metal Pt and Pt-based materials have shown the remarkable ORR activity (Chen et al., 2018; He et al., 2015; Jiang et al., 2017), but their scarcity and high cost constrain the commercial application of this technology (Chung et al., 2013). Therefore, it is desired to develop alternatives with high catalytic activity and low-cost.

Extensive studies have found that activated carbon (AC) with plenty, low-cost and high surface area has better electrocatalytic activity compared to other materials (Dong et al., 2012; Santoro et al., 2014). Nevertheless, the power density is much lower than the conventional Pt or Pt-based catalysts. Hence, it is essential to explore new catalyst to modify AC, further enhancing the power output of activated carbon air-cathode MFC (Zhang et al., 2014b). Transition metals (Co, Fe and Ni) and their oxides exhibited remarkable electrochemical activity for oxygen reduction (Liu et al., 2016). However, owing to their low surface area and insufficient conductivity, it's essential to combine pure metal and carbon nanomaterials, such as carbon nanotube or grapheme to solve these problems. Carbon based nanocomposites have been investigated as excellent ORR electrocatalysts, especially non-noble metal-containing carbon materials (Masa et al., 2014). Recently, metal-organic framework (MOF) has emerged as template for the synthesis of nanocarbon composites (Liu et al., 2008; Wang et al., 2013). Zeolitic

* Corresponding authors.
E-mail addresses: tdxjwang@163.com (X. Wang), likx@nankai.edu.cn (K. Li).
[1] Author S. Zhang and W. Su contributed equally to this work.

https://doi.org/10.1016/j.bios.2018.12.028
Received 16 October 2018; Received in revised form 11 December 2018; Accepted 16 December 2018
Available online 21 December 2018
0956-5663/

imidazolate framework (ZIF), a subclass of MOF, is selected as precursor in view of the coexistence of abundant carbon and nitrogen species (Palaniselvam et al., 2013; Zhang et al., 2013). You et al. reported that ZIF-67-derived electrocatalyst containing cobalt and nitrogen-doped carbon achieved the maximum power density of 1665 mW m^{-2} in MFC (You et al., 2016). Besides, Tang et al. found that a class of Co-MOF-derived dual metal and nitrogen codoped carbon exhibited advanced ORR performance (Tang et al., 2016). However, to our knowledge, the strategy for encapsulating metal nanoparticles into nitrogen-doped carbon nanotubes nanopolyheda is rarely reported in activated carbon air-cathode MFC.

Herein, nitrogen-doped carbon nanotube nanopolyheda embedded cobalt nanoparticles catalyst was synthesized via a facile pyrolysis bimetallic metal-organic frameworks (ZnCo-ZIFs) process. The as-prepared electrocatalyst combined high specific surface area, complex textural properties, transition metal element and nitrogen chemical state, hence resulting in superior ORR activity and remarkable power generation. Furthermore, comprehensive characterizations and detailed experimental analyses were conducted to thoroughly investigate the MFC performance.

2. Material and methods

2.1. Synthesis of Co-NCNTNP

All chemicals used in this work were in analytical grade and used without further purification. The synthesis procedure of the Co-NCNTNP was similar to a reported method with minor modification (Chen et al., 2017). Typically, 5 mmol of $Co(NO_3)_2{\cdot}6H_2O$ and 10 mmol of $Zn(NO_3)_2{\cdot}6H_2O$ were dissolved in 150 mL methanol. Then the solution was quickly poured into a methanol solution of 2-methylimidazole (4.92 g, 50 mL) with vigorous stirring for 30 mins. The mixture was stirred for 24 h at room temperature and the violet powdery precipitate was collected by centrifugation, followed by thorough washing with methanol, and then dried in a vacuum oven at 60 °C for 12 h to obtain the uniform polyhedral ZnCo-ZIFs. The as-synthesized ZnCo-ZIFs were then calcined at 800 °C for 3 h in a tube furnace under Ar/H_2 flow with a heating rate of 2 °C/min and the black powders (Co-NCNTNP) were collected finally by washing with deionized water for several times.

2.2. Preparation of the air-cathode

All the cathodes were fabricated via the rolling-press method as previously studied (Dong et al., 2012). Stainless steel mesh was prepared as cathode treated with two layers on facing air sides called gas diffusion layer and as-synthesized material on another side called catalyst layer. Typically, the catalyst layer facing solution was prepared by mixing Co-NCNTNP electrocatalyst with activated carbon (2100 m^2 g^{-1}, Yihuan Carbon Co. Ltd., Fujian, China) and polytetrafluoroethylene (PTFE, 60 wt%, Hesen, Shanghai, China) with a mass ratio of 6:1. The different contents of Co-NCNTNP in the catalyst layer were 0 wt%, 3 wt%, 5 wt%, 10 wt% and 15 wt%, and the final products were renamed as bare AC, AC-Co-NCNT-1, AC-CoNCNT-2, AC-CoNCNT-3 and AC-CoNCNT-4, respectively. The gas diffusion layer facing air was made by rolling carbon black (Jinqiushi Chemical Co. Ltd., Tianjin, China) and PTFE with a mass ratio of 3:7 and then sintered in the muffle furnace at 340 °C for 20 min. Then the cathode was dried at 30 °C for 12 h to remove the residual solvent.

2.3. Construction and operation of MFC

The single-chamber air cathode MFC was fabricated with transparent Plexiglas with a working volume of 28 mL (4 cm electrode spacing and 3 cm diameter). The anode was carbon felt which was soaked in acetone for 12 h and then washed four times with deionized water. Both electrodes were connected by titanium wire along with a resistance of 1 kΩ. All the tested MFCs were operated in biochemical incubator, inoculated with the mixtures of the domestic wastewater, 50 mM phosphate buffered saline (PBS), 12.5 mL L^{-1} trace minerals and 5 mL L^{-1} vitamins. After four cycle (each cycle lasted about 2 days), the medium was switched to PBS and acetate solution (2 g L^{-1}) only. During the operation, the voltage was recorded instantaneously by the data acquisition card (Morpheus Electronic Co. Ltd, Beijing, China).

2.4. Electrochemical and structural characterization

The power density and polarization curves of MFCs were obtained with the external resistance varying from 9000 to 70 Ω. The ORR performance was investigated by linear sweep voltammetry (LSV), electrochemical impedance spectroscopy (EIS) and Tafel plots in 50 mM PBS (pH = 7) at room temperature. All the electrochemical experiments were conducted in a three-electrode system by using an advanced electrochemical workstation (VersaSTAT 3, Princeton Applied Research, USA). The as-prepared cathode was used as the working electrode. Ag/AgCl and platinum sheet (1 cm^2) were used as reference electrode and counter electrode, respectively. LSV was tested at a scan rate of 0.1 mV s^{-1}, within a potential range from open circuit potential (OCP) to − 0.3 V. EIS was carried out in a wide frequency range of 100 kHz to 10 mHz at OCP. Exchange current density (i_0, A cm^{-2}) measurement was conducted over the overpotential from 0 to 100 mV with a scan rate of 1 mV s^{-1}. i_0 was calculated by the following Tafel equation: $\lg i = \lg i_o - \beta nF\eta/2.303RT$ (Dong et al., 2012). Rotating disk electrode (RDE-3A, ALS, Japan) was employed to deeply understand the electrocatalytic performance of the Co-NCNTNP catalyst during the ORR process. 4 mg as-prepared material was ultrasonically dispersed into 5 mL ethanol and 1 mL 0.05 wt% Nafion solution to form a catalyst ink. Appropriate amount of the catalyst ink (about 2 μL) was dripped on the glassy carbon electrode and then dried at the room temperature. ORR measurement was performed in the O_2-saturated PBS via linear scanning from 0.3 to − 1.0 V at a scan rate of 5 mV s^{-1} with different rotation rates (625, 900, 1225, 1600, 2000 and 2500 rpm) (Goh et al., 2013).

The powder X-ray diffraction (XRD) was performed on a Bruker D8 advanced X-ray diffractometer with Cu Kα radiation to characterize the crystallinity of the sample. The X-ray photoelectron spectroscopy (XPS, ESCALAB 250 XI, Thermo Scientific, USA) spectra was conducted to analyze the surface elements and their chemical bonding states of the Co-NCNTNP, and the final spectra was calibrated to the adventitious carbon C1s peak at 284.8 eV. The specific surface area and pore size distribution of the as-synthesized electrocatalyst was calculated using the Brunauer-Emmett-Teller (BET) method with an adsorption meter (ASAP 2460, Micromeritics, USA). The morphology of the prepared sample was characterized with field emission scanning electron microscopy (FESEM, Hitachi, JSM-7610F), high resolution transmission electron microscopy (HRTEM, JEOL, JEM-2100F). Elemental mapping was conducted using EDAX detector attached on JEM-2100F. The Raman spectra was obtained using a Renishaw InVia Reflex spectrometer 2000, operating with a visible laser beam of 633 nm.

3. Results and discussion

3.1. Structural characterization of Co-NCNTNP

The synthesis procedure of the Co-NCNTNP was illustrated in Fig. 1a. Bimetallic zeolitic imidazolate frameworks ZnCo-ZIFs were obtained firstly via the room-temperature reaction of $Zn(NO_3)_2$ and $Co(NO_3)_2$ mixture solution and 2-methylimidazole in methanol. Afterward, reductive pyrolysis under Ar/H_2 flow was applied to form the Co-NCNTNP catalyst. The porous structure coupled with nitrogen-doped carbon nanotubes was produced owing to the evaporation of Zn during the pyrolysis process. The XRD patterns of precursor ZnCo-ZIFs and Co-

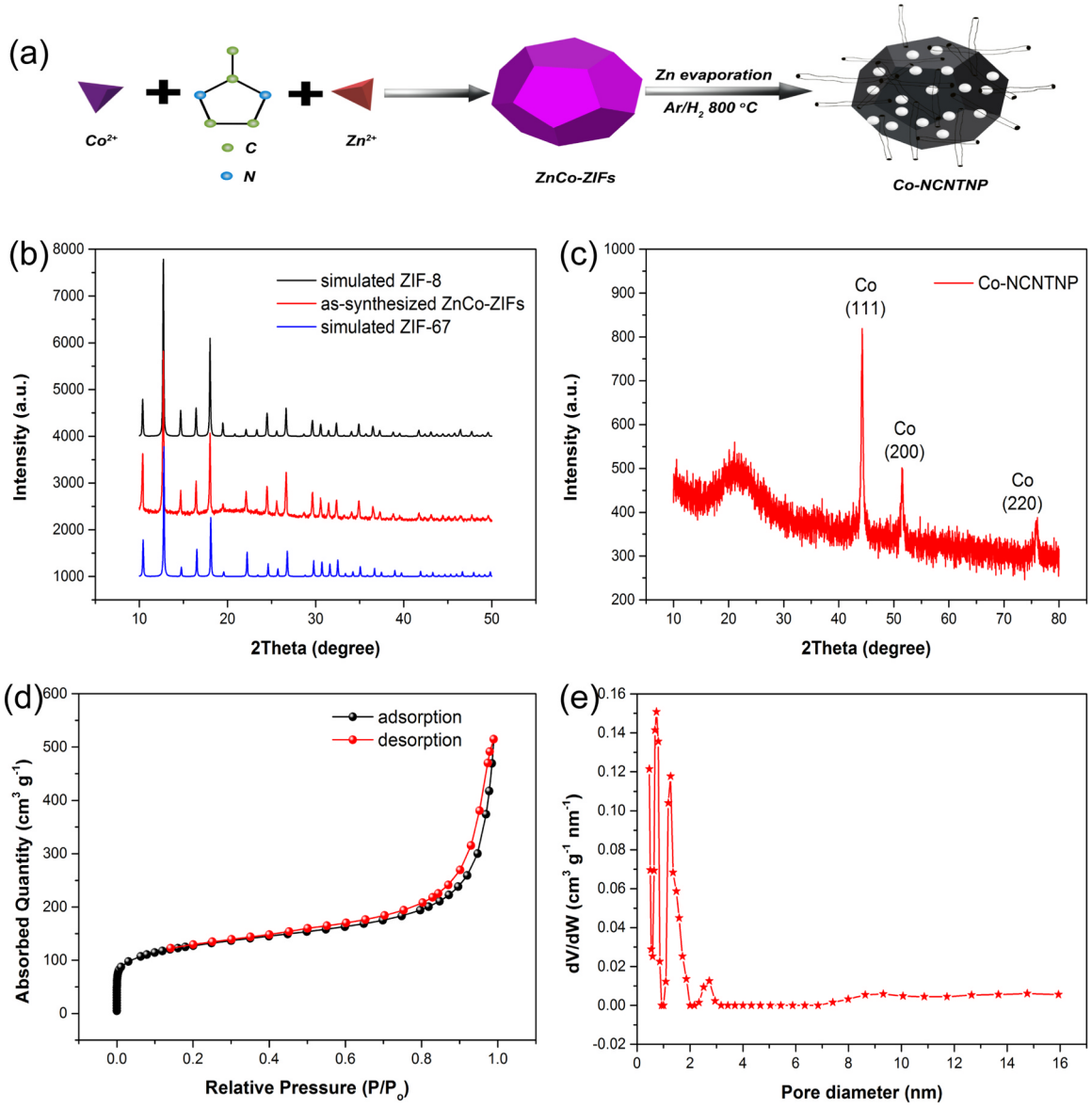

Fig. 1. (a) Synthesis procedure of the Co-NCNTNP; (b, c) XRD patterns of the as-synthesized ZnCo-ZIFs and Co-NCNTNP and (d, e) Nitrogen adsorption-desorption isotherm loop and corresponding pore size distribution curve of Co-NCNTNP.

NCNTNP were depicted in Fig. 1b and Fig. 1c, respectively. Fig. 1b indicated that the as-synthesized ZnCo-ZIFs matched well with simulated ZIF-8 and ZIF-67 because of their similar unit cells and crystal lattices. Fig. 1c showed three typical characteristic diffraction peaks around 44.2°, 51.5° and 75.9°, in good agreement with the (111), (200) and (220) lattice planes of Co nanoparticles (JCPDS No: 15-0806), respectively (Liu et al., 2017). Additionally, the broad diffraction peak at around 23°, corresponding to the disordered carbon (Wu et al., 2014). The textural properties of the as-synthesized Co-NCNTNP were evaluated by the Nitrogen adsorption-desorption characterization. As shown in Fig. 1d, it presented the joint of the type I and IV isotherms, indicating the existence of both micropores and mesopores. The surface area of the Co-NCNTNP was calculated to be 463.47 m^2 g^{-1} using Brunauer-Emmett-Teller (BET) method, much larger than that of the Co@NCNT (97.4 m^2 g^{-1}) synthesized by pyrolysis of the mixture of ZIF-67 and dicyandiamide (Zhang et al., 2016a). The pore size distribution plot indicated that the Co-NCNTNP nanocatalyst possessed ultramicropore, micropore and mesopore centred at 0.73, 1.26 and 2.73 nm, respectively (Fig. 1e), according the nonlocal density functional theory. The coexistence of micro-mesoporous structure of the Co-NCNTNP was believed to be beneficial combination for ORR, owing to the micropores providing greater number of accessible active sites while the mesopores accelerating the mass transport in the catalyst layer (Liang et al., 2014). The intensity ratios (I_D/I_G) of Co-NCNTNP and bare AC, conducted by Raman spectroscopy, were calculated to be 1.20 and 1.12, respectively (Fig. S1). It was reported that the higher I_D/I_G indicated the transition metal particles have facilitated the incorporation of N atoms to the carbon framework to distort the graphitic framework, forming greater positive sites on the adjacent carbon atoms to adsorb oxygen, which contributed to the enhanced ORR activity (Ghanbarlou et al., 2015; Karunagaran et al., 2018).

FESEM and HR-TEM were employed to investigate the morphology of the precursor ZnCo-ZIFs and as-synthesized Co-NCNT. FESEM images (Fig. S2a, b) revealed that the ZnCo-ZIFs possessed well-defined polyhedral shape with an average size of approximately 400 nm. After a pyrolysis process at 800 °C for 3 h under the reductive atmosphere, the ZnCo-ZIFs were converted to N-doped porous carbon frameworks with embedded Co nanoparticles and carbon nanotubes, as shown in Fig. 2a, b and Fig. S2c, d. Additionally, Co nanoparticles and carbon nanotubes were further revealed by HR-TEM observations (Fig. 2c and Fig. 2d). It

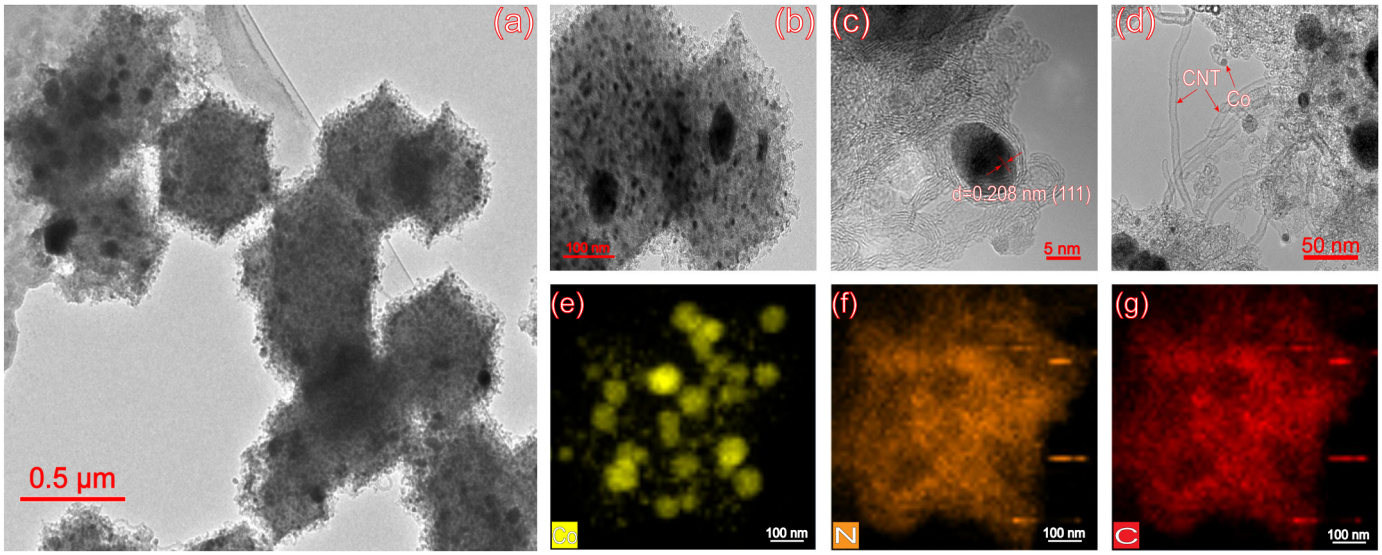

Fig. 2. (a) FESEM image of ZnCo-ZIFs-derived Co-NCNTNP; (b)HR-TEM image of the Co-NCNTNP; (c) The Co nanoparticles wrapped by the carbon nanotube; (d) The carbon nanotubes from the HR-TEM images of the Co-NCNTNP; (e-g) Elemental mappings of Co, N and C in the Co-NCNTNP.

has been previously reported that electrocatalysts possessed enhanced activity in the presence of metallic nanoparticles owing to the electronic interaction between metal nanoparticles and carbon nanotubes (G et al., 2011; Lefèvre et al., 2009). Fig. 2c showed a crystal lattice spacing of 0.208 nm, associated to the (111) plane of Co nanoparticle, which was consistent with XRD findings (Li et al., 2016). Elemental mapping images of Co-NCNTNP indicated the Co, N and C were well dispersed in the carbon framework, presented in Fig. 2e, Fig. 2f and Fig. 2g, respectively.

XPS was utilized to probe the chemical composition and element bonding configuration in Co-NCNTNP. The coexistence of Co, N and C in catalyst was presented in Fig. S3a. The C 1s spectrum (Fig. S3d) revealed the presence of C=C bond (284.4 eV) and C=N bond (285.3 eV) (Chen et al., 2017). The high-resolution Co 2p spectrum, shown in Fig. S3b, deconvoluted into two types of cobalt species containing metallic Co nanoparticles (777.8 eV) and Co-Nx (779.9 eV) (Xiang et al., 2014). Chen et al. found that the catalyst embedded Co nanoparticles exhibited faster electrochemical reaction kinetics (Chen et al., 2017). Han et al. also reported that high ORR electrochemical activity of the catalyst was attributed to the single Co site, which could accelerate the proton and charge transfer at interface (Han et al., 2017). Additionally, chao et al. reasoned that the Co-N_x active sites were beneficial to ORR (Chao et al., 2015). The N 1 s spectrum (Fig. S3c) showed three peaks at 398.6 eV, 400.7 eV and 401.4 eV, corresponding to pyridinic N, Co-N_x and graphitic N, respectively (Liu et al., 2010, 2013). Pyridinic N and graphitic N have been considered to be favorable for the improvement of ORR activity (He et al., 2014; Shang et al., 2015). Thus, we can conclude that the excellent electrocatalytic activity of the Co-NCNTNP for ORR was mainly ascribed to the synergistic effect of Co nanoparticles, Co-N_x active site, Pyridinic N and graphitic N.

3.2. Performance of MFC

To get a stable electricity generation performance, the power density and polarization curves were obtained after a month of continuously cultivation. The polarization curves illustrated that the anode potentials of all tested MFCs were almost same (Fig. 3b), while the cathode potentials decreased along with increased current densities, indicating the cathode performance was dominated factor for the energy output of MFCs. The power density curves displayed that the MFCs equipped with the as-synthesized Co-NCNTNP catalyst reached higher maximum power densities (MPD) than that of control (Fig. 3a). To be specific, MFC equipped with AC-CoNCNT-3 cathode got the MPD of 2252 ± 46 mW m^{-2}, 1.19, 1.49, 1.62 and 2.54 times as high as that of AC-CoNCNT-4 (1893 ± 55 mW m^{-2}), AC-CoNCNT-2 (1509 ± 60 mW m^{-2}), AC-CoNCNT-1 (1390 ± 54 mW m^{-2}) and bare AC (888 ± 56 mW m^{-2}), respectively. Moreover, this value was much higher than that of Pt/C cathode with electrodeposition (1260 ± 60 mW m^{-2}) (Fig. S4). Therefore, the above results suggested that Co-NCNTNP had a better electrocatalytic activity in MFCs.

Compared with the recent researches, the MPD produced by the 10% Co-NCNTNP modified AC cathode was much higher than that of carbon nanotube supported MnO_2 (97.8 mW m^{-2}) (Chindaprasirt and Sawanyawisuth, 2011), cobalt oxide/nanocarbon hybrid material (467 ± 17 mW m^{-2}) (Song et al., 2015) and nickel oxide and carbon nanotube composites (670 mW m^{-2}) (Huang et al., 2015). In addition, You et al. found the metal organic framework-derived electrocatalyst containing cobalt and nitrogen-doped carbon (CoNC) exhibited enhanced activity towards ORR, and the optimized CoNC got the MPD of 1665 mW m^{-2}, 35% lower than that of AC-CoNCNT-3 (You et al., 2016). To our knowledge, MFC equipped with Co-NCNTNP modified activated carbon cathode exhibited remarkable performance compared to the state-of-the-art catalysts Fe_3O_4 (Fu et al., 2015), Co_3O_4 (Ge et al., 2015), MnO_2 (Zhang et al., 2014a), $NiCo_2O_4$ (Ge et al., 2016). Hence, we can conclude that as-synthesized Co-NCNTNP would be a good alternative catalyst in air-cathode microbial fuel cell application.

3.3. Electrochemical characterization of air cathode

LSV was conducted to estimate the effect of Co-NCNTNP toward ORR, shown in Fig. 4a. The open circuit potential (OCP) and current densities of cathodes modified by Co-NCNTNP catalyst were increased remarkably. Specifically, the OCP of AC-Co-NCNT-3 was measured to be 0.297 V, 67.80% higher than that of bare AC (0.177 V). And AC-CoNCNT-4, AC-CoNCNT-2 and AC-CoNCNT-1 were tested to be 0.280 V, 0.263 V, and 0.229 V, respectively, 58.20%, 48.59% and 29.38% higher than that of bare AC, respectively. Besides, the potential between 0.1 and −0.1 V was deem as most critical index of these air cathodes. At the potential of −0.1 V, the current densities of all tested cathodes were ordered as follows: AC-CoNCNT-3 (9.22 mA cm^{-2}) > AC-CoNCNT-4 (8.45 mA cm^{-2}) > AC-CoNCNT-2 (7.29 mA cm^{-2}) > AC-CoNCNT-1 (5.98 mA cm^{-2}) > bare AC (4.08 mA cm^{-2}), which indicated the modification of Co-NCNTNP was beneficial to improving the electrochemical performance. Moreover, the AC-

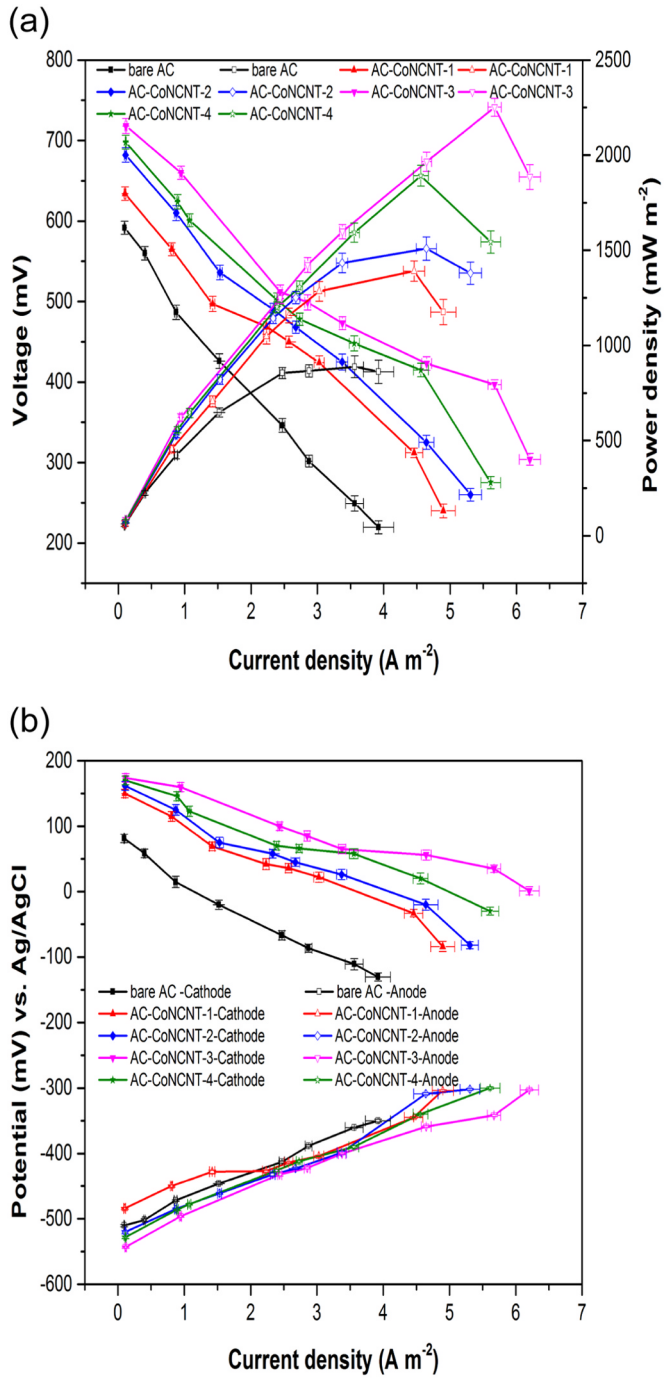

Fig. 3. Performance of MFC equipped with different air cathodes. (a) Power density and cell voltage curves and (b) Cathode and anode polarization curves.

CoNCNT-3 possessed highest OCP and current density exhibited the best performance among all the tested cathodes. Hence, LSV results suggested that the procedure using as-prepared Co-NCNTNP catalyst to modify AC air-cathode was positive.

EIS analysis was employed to further understand the electrochemical behavior of air cathodes and the Nyquist plots were shown in Fig. 4b. The equivalent circuit, adopted a reported EIS model (Zhang et al., 2011), included a resistance of electrolyte solution (R_0), a charge transfer resistance (R_{ct}) and a diffusion resistance (R_d). From the plots, we found that the resistance of air cathodes equipped with as-prepared Co-NCNTNP catalyst decreased obviously, indicating electrochemical activity was improved significantly. The calculated resistances, listed in Table S1, demonstrated the value of R_{ct} for AC-CoNCNT-1, AC-CoNCNT-2, AC-CoNCNT-3 and AC-CoNCNT-4 were 1.745 Ω, 1.68 Ω, 1.134 Ω, and 1.416 Ω, respectively, much smaller than that of bare AC cathode (2.346 Ω). The decreased R_{ct} might be explained by the single Co site because of it could accelerate the proton and charge transfer at interface. Furthermore, previous research have reported that a smaller R_{ct} implied a faster electron rate (Wen et al., 2012). Additionally, the R_d of AC air-cathode (3.202 Ω) was much higher than that of AC-CoNCNT-3 (0.845 Ω). The decreased R_d may be ascribed to the textural features of as-prepared Co-NCNTNP. Jiang et al. reasoned that the large pore size could minimize the diffusion resistance, which was beneficial to acceleration of ion diffusion (Jiang et al., 2012). Moreover, the total resistance ($R_o + R_{ct} + R_d$) order of all cathodes was bare AC (18.088 Ω) > AC-CoNCNT-1 (17.292 Ω) > AC-CoNCNT-2 (12.854 Ω) > AC-CoNCNT-4 (11.312 Ω) > AC-CoNCNT-3 (10.609 Ω). Both LSV and EIS results suggested that the cathode equipped with as-synthesized Co-NCNTNP catalyst exhibited improved eletrocatalytic activity towards ORR. Therefore, Co-NCNTNP modified air-cathodes exhibited remarkable power output than that of control.

3.4. Catalysis kinetics on ORR

Tafel equation was used to determine the exchange current density (i_o). The Tafel plots of all cathodes were shown in Fig. 4c and a linear regression with $R^2 > 0.99$ was extracted from the overpotential of 60–80 mV (Fig. 4d). The linear fitting equation and i_o were given in Table 1. We found that the i_o values increased from 8.413×10^{-4} A cm^{-2} (bare AC) to 18.745×10^{-4} A cm^{-2} (AC-CoNCNT-3). Previous study reasoned that the increase of i_o contributed to accelerating reaction rate and utilizing the electrons more effectively (Jadhav et al., 2014). Additionally, this result was consistent with the LSV and EIS analyses. Thus, it was clearly shown that activated carbon air-cathodes modified by the Co-NCNTNP catalyst exhibited a higher i_o than that of control, indicating a faster rate of electron transfer, which finally contributed to the improved performance.

RDE measurements were conducted to further asses the ORR electron-transfer mechanism. Fig. 4**e** displayed the increasing current densities with increasing rotating speeds. The calculated electron transfer numbers (n) for as-prepared catalyst Co-NCNTNP at different potentials were in the range of 3.64–3.81 (Fig. 4**f**). The higher n implied a more effective pathway to reduce oxygen. Zhang et al. found that the electron transfer number of Co@NCNT derived from ZIF-67 and dicyandiamide was 3.90 for ORR (Zhang et al., 2016b). Hao et al. reported that the electron number was around 3.90 for the bamboo-like nitrogen doped carbon nanotubes with embedded Co nanoparticles fabricated by a one-step pyrolysis method (Hao et al., 2017). Therefore, the above results suggested that as-synthesized Co-NCNTNP catalyst exhibited a desired four-electron process towards ORR like Pt/C.

4. Conclusions

Benefiting from the unique architectural features, cobalt nanoparticles embedded in N-doped carbon nanotube nanopolyhedra, synthesized via a facile method of pyrolysis bimetallic metal-organic frameworks, exhibited outstanding ORR activity. When firstly used to modify the activated carbon air-cathode of MFC, the maximum power density increased by 154% compared to that of control. Moreover, electrochemical measurements demonstrated the Co-NCNTNP exhibited an efficient four-electron pathway of oxygen reduction like Pt/C. Therefore, these attractive properties suggested that the Co-NCNTNP would be a promising Pt-alternative electrocatalyst for air-cathode MFC. However, the further work should be continued to prove that the as-synthesized electrocatalyst could be a good candidate for commercial application.

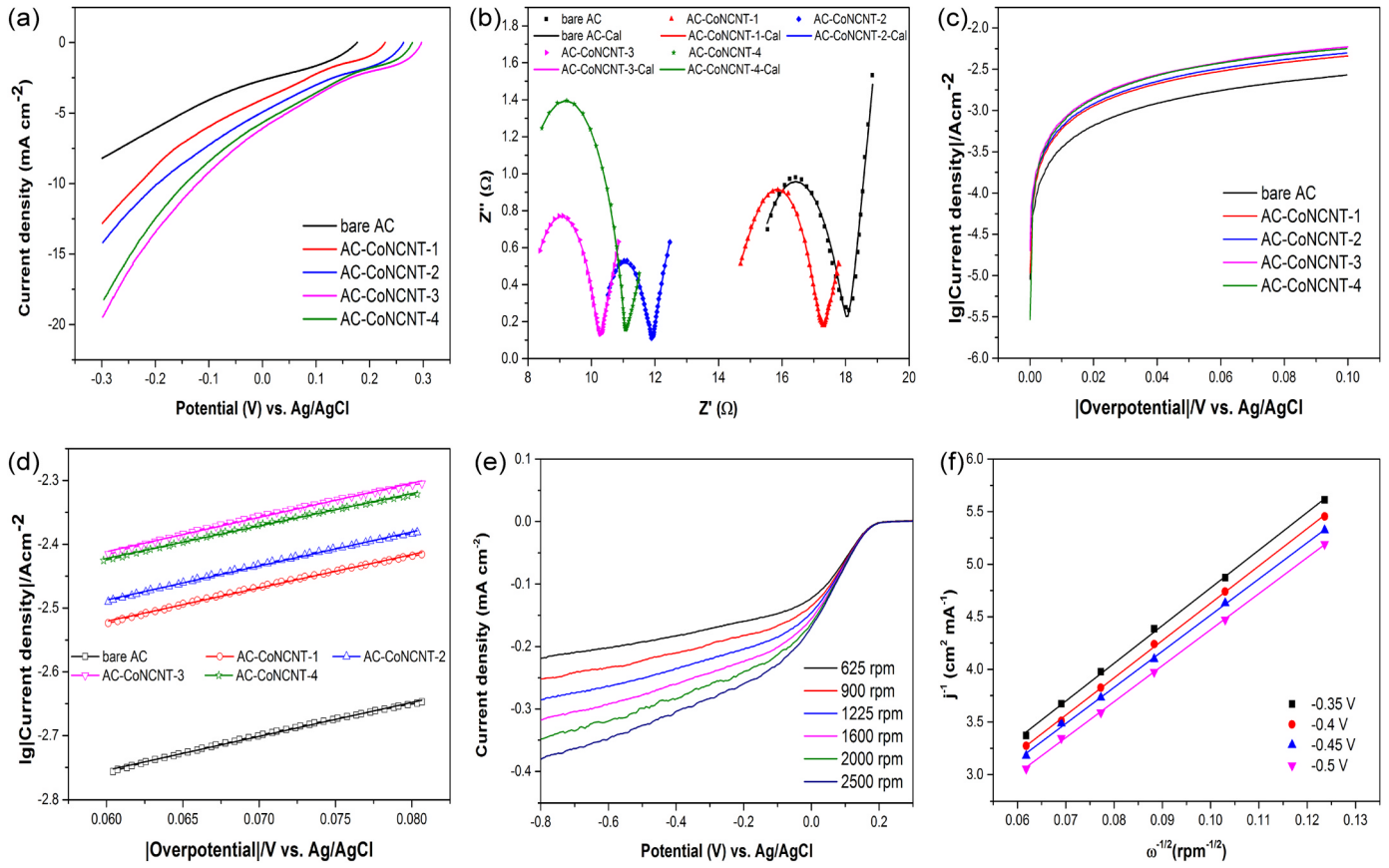

Fig. 4. (a) LSVs of the bare AC and Co-NCNTNP modified AC cathodes; (b) Nyquist plots of EIS of bare AC and Co-NCNTNP modified AC cathodes. Lines marked as 'Cal' were fitting data from the equivalent circuit; (c) Tafel plots of the bare AC and Co-NCNTNP modified AC cathodes; (d) The linear fit for the Tafel plots of overpotential from 60 to 80 mV; (e) Rotating-disk voltammogram result of the Co-NCNTNP in O_2 saturated electrode and (f) Corresponding K-L plots at different potentials.

Table 1
Exchange current density calculated from the Tafel plots.

The air-cathode	Linear fitting equation (R^2)	10^{-4} i_o (A cm^{-2})
bare AC	y = −3.07506 + 5.34082x(0.99759)	8.413
AC-CoNCNT-1	y = −2.83465 + 5.23073x(0.9973)	14.634
AC-CoNCNT-2	y = −2.80737 + 5.33342x(0.99791)	15.582
AC-CoNCNT-3	y = −2.72712 + 5.08259x(0.99769)	18.745
AC-CoNCNT-4	y = −2.73392 + 5.37186x(0.9962)	18.454

CRediT authorship contribution statement

Song Zhang: Writing - original draft. **Wei Su:** Writing - original draft. **Xiaojing Wang:** Conceptualization, Formal analysis. **Kexun Li:** Conceptualization, Formal analysis. **Yong Li:** Project administration.

Acknowledgements

This work was supported by the Natural Science Foundation of Tianjin Municipal Science and Technology Commission (17JCYBJC23300) and National Key R&D Program of China (No. 2016YFC0400704 and No. 2016YFC0401407). In addition, International Clean Energy Talent Programme (ICET) also subsidized this paper.

Declaration of interests

The authors declare that they have no known competing financial interests or personal relationships that could have appeared to influence the work reported in this paper.

Appendix A. Supporting information

Supplementary data associated with this article can be found in the online version at doi:10.1016/j.bios.2018.12.028.

References

Chao, S., Bai, Z., Cui, Q., Yan, H., Wang, K., Yang, L., 2015. Carbon 82, 77–86.
Chen, T., Cheng, B., Zhu, G., Chen, R., Hu, Y., Ma, L., Lv, H., Wang, Y., Liang, J., Tie, Z., 2017. Nano Lett. 17 (1), 437–444.
Chen, X.L., Zhang, H., Huang, X.Y., Feng, J.J., Han, D.M., Zhang, L., Chen, J.R., Wang, A.J., 2018. J. Colloid Interface Sci. 525, 260–268.
Chindaprasirt, J., Sawanyawisuth, K., 2011. Biosens. Bioelectron. 26 (12), 4728–4732.
Chung, H.T., Won, J.H., Zelenay, P., 2013. Nat. Commun. 4 (5), 1922.
Dong, H., Yu, H., Wang, X., Zhou, Q., Feng, J., 2012. Water Res. 46 (17), 5777–5787.
Fan, Y., Han, S.K., Liu, H., 2012. Environ. Sci. 5 (8), 8273–8280.
Fu, Z., Yan, L., Li, K., Ge, B., Pu, L., Zhang, X., 2015. Biosens. Bioelectron. 74, 989–995.
G, W., KL, M., CM, J., P, Z., 2011. Science 332 (6028), 443–447.
Ge, B., Li, K., Fu, Z., Pu, L., Zhang, X., 2015. Bioresour. Technol. 195, 180–187.
Ge, B., Li, K., Fu, Z., Pu, L., Zhang, X., Liu, Z., Huang, K., 2016. J. Power Sources 303, 325–332.
Ghanbarlou, H., Rowshanzamir, S., Kazeminasab, B., Parnian, M.J., 2015. J. Power Sources 273, 981–989.
Goh, F.W.T., Liu, Z., Ge, X., Zong, Y., Du, G., Hor, T.S.A., 2013. Electrochim. Acta 114 (114), 598–604.
Han, Y., Wang, Y.G., Chen, W., Xu, R., Li, R.Z., Jian, Z., Luo, J., Shen, R.A., Zhu, Y., Cheong, W.C., 2017. J. Am. Chem. Soc. 139, 17269–17272.
Hao, Y., Lu, Z., Zhang, G., Chang, Z., Luo, L., Sun, X., 2017. Energy Technol. 5 (8), 1265–1271.
He, L.-L., Song, P., Wang, A.-J., Zheng, J.-N., Mei, L.-P., Feng, J.-J., 2015. J. Mater. Chem. A 3 (10), 5352–5359.
He, W., Jiang, C., Wang, J., Lu, L., 2014. Angew. Chem. Int. Ed. 53 (36), 9503–9507.
Huang, J.J., Zhu, N.W., Yang, T.T., Zhang, T.P., Wu, P.X., Dang, Z., 2015. Biosens. Bioelectron. 72, 332–339.
Jadhav, D.A., Ghadge, A.N., Mondal, D., Ghangrekar, M.M., 2014. Bioresour. Technol. 154 (2), 330–335.

Jiang, Huang, X.Y., Wang, A.J., et al., 2017. J. Mater. Chem. A 5 (21), 10554–10560.
Jiang, H., Ma, J., Li, C., 2012. Chem. Commun. 48 (37), 4465–4467.
Karunagaran, R., Coghlan, C., Shearer, C., Tran, D., Gulati, K., Tung, T.T., Doonan, C., Losic, D., 2018. Materials 11 (2), 205.
Lefèvre, M., Proietti, E., Jaouen, F., Dodelet, J.P., 2009. Science 324 (5923), 71–74.
Li, Z., Li, C., Ge, X., Ma, J., Zhang, Z., Li, Q., Wang, C., Yin, L., 2016. Nano Energy 23, 15–26.
Liang, H.W., Zhuang, X., Brüller, S., Feng, X., Müllen, K., 2014. Nat. Commun. 5 (5), 4973.
Liu, Jiang, H., Zhu, Y., et al., 2016. J. Mater. Chem. A 4 (5), 1694–1701.
Liu, B., Shioyama, H., Akita, T., Xu, Q., 2008. J. Am. Chem. Soc. 130 (16), 5390–5391.
Liu, R., Wu, D., Feng, X., Müllen, K., 2010. Chem. Int. Ed. 49 (14), 2565–2569.
Liu, S., Wang, Z., Si, Z., Yu, F., Yu, M., Chiang, C.Y., Zhou, W., Zhao, J., Qiu, J., 2017. Adv. Mater. 29 (31), 1700874.
Liu, Z., Zhang, G., Lu, Z., Jin, X., Chang, Z., Sun, X., 2013. Nano Res. 6 (4), 293–301.
Masa, J., Xia, W., Sinev, I., Zhao, A., Sun, Z., Grützke, S., Weide, P., Muhler, M., Schuhmann, W., 2014. Angew. Chem. Int. Ed. 53 (32), 8508–8512.
Palaniselvam, T., Biswal, B.P., Banerjee, R., Kurungot, S., 2013. Chem 19 (28), 9335–9342.
Qiao, Y., Bao, S., Li, C.M., 2010. Energ. Environ. Sci. 3 (5), 544–553.
Santoro, C., Babanova, S., Artyushkova, K., Atanassov, P., Greenman, J., Cristiani, P., Trasatti, S., Schuler, A.J., Li, B., Ieropoulos, I., 2014. Int. J. Hydrog. Energy 39 (36), 21796–21802.
Shang, L., Yu, H., Huang, X., Bian, T., Shi, R., Zhao, Y., Waterhouse, G.I., Wu, L.Z., Tung, C.H., Zhang, T., 2015. Adv. Mater. 28 (8), 1668–1674.
Song, T.S., Wang, D.B., Wang, H., Li, X., Liang, Y., Xie, J., 2015. Int. J. Hydrog. Energy 40 (10), 3868–3874.
Tang, H., Cai, S., Xie, S., Wang, Z., Tong, Y., Pan, M., Lu, X., 2016. Adv. Sci. 3 (2), 1487–1498.
Wang, C., Liu, D., Lin, W., 2013. J. Am. Chem. Soc. 135 (36), 13222–13234.
Wen, Q., Wang, S., Yan, J., Cong, L., Pan, Z., Ren, Y., Fan, Z., 2012. J. Power Sources 216 (216), 187–191.
Wu, Y., Gao, M., Li, X., Liu, Y., Pan, H., 2014. J. Alloy. Compd. 608, 220–228.
Xiang, Z., Xue, Y., Cao, D., Huang, L., Chen, J.F., Dai, L., 2014. Angew. Chem. Int. Ed. 126 (9), 2465–2469.
You, S., Gong, X., Wang, W., Qi, D., Wang, X., Chen, X., Ren, N., 2016. Adv. Energy Mater. 6 (1), 1501497.
Zhang, E., Xie, Y., Ci, S., Jia, J., Cai, P., Yi, L., Wen, Z., 2016a. J. Mater. Chem. A 4 (44), 17288–17298.
Zhang, E., Xie, Y., Ci, S., Jia, J., Cai, P., Yi, L., Wen, Z., 2016b. J. Mater. Chem. A 4 (44), 17239–17574.
Zhang, F., Pant, D., Logan, B.E., 2011. Biosens. Bioelectron. 30 (1), 49–55.
Zhang, P., Sun, F., Xiang, Z., Shen, Z., Yun, J., Cao, D., 2013. Energy Environ. Sci. 7 (1), 442–450.
Zhang, P., Li, K., Liu, X., 2014a. J. Power Sources 264 (9), 248–253.
Zhang, X., Pant, D., Zhang, F., Liu, J., He, W., Logan, B.E., 2014b. Chemelectrochem 1 (11), 1859–1866.
Zhu, N., Huang, J., Shen, W., Tu, L., Wu, P., Ma, H., 2015. Int. J. Electrochem. Sci. 10 (3), 2634–2645.